




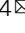



Ultrasensitive barocaloric material for room-temperature solid-state refrigeration

Qingyong Ren ^{1,2,6}, Ji Qi^{3,4,6}, Dehong Yu ⁵, Zhe Zhang^{3,4}, Ruiqi Song³, Wenli Song^{1,2}, Bao Yuan^{1,2}, Tianhao Wang^{1,2}, Weijun Ren³, Zhidong Zhang ^{3,4}, Xin Tong^{1,2}  & Bing Li ^{3,4} 

One of the greatest obstacles to the real application of solid-state refrigeration is the huge driving fields. Here, we report a giant barocaloric effect in inorganic NH_4I with reversible entropy changes of $\Delta S_{p_0 \rightarrow p}^{\text{max}} \sim 71 \text{ J K}^{-1} \text{ kg}^{-1}$ around room temperature, associated with a structural phase transition. The phase transition temperature, T_t , varies dramatically with pressure at a rate of $dT_t/dP \sim 0.79 \text{ K MPa}^{-1}$, which leads to a very small saturation driving pressure of $\Delta P \sim 40 \text{ MPa}$, an extremely large barocaloric strength of $|\Delta S_{p_0 \rightarrow p}^{\text{max}}/\Delta P| \sim 1.78 \text{ J K}^{-1} \text{ kg}^{-1} \text{ MPa}^{-1}$, as well as a broad temperature span of $\sim 41 \text{ K}$ under 80 MPa. Comprehensive characterizations of the crystal structures and atomic dynamics by neutron scattering reveal that a strong reorientation-vibration coupling is responsible for the large pressure sensitivity of T_t . This work is expected to advance the practical application of barocaloric refrigeration.

¹Institute of High Energy Physics, Chinese Academy of Sciences, Beijing 100049, China. ²Spallation Neutron Source Science Center, Dongguan 523803, China. ³Shenyang National Laboratory for Materials Science, Institute of Metal Research, Chinese Academy of Sciences, 72 Wenhua Road, Shenyang 110016, China. ⁴School of Materials Science and Engineering, University of Science and Technology of China, 72 Wenhua Road, Shenyang 110016, China. ⁵Australian Nuclear Science and Technology Organisation, Lucas Heights, New South Wales 2234, Australia. ⁶These authors contributed equally: Qingyong Ren, Ji Qi. email: tongx@ihep.ac.cn; bingli@imr.ac.cn

To tackle climate change and realize the United Nations' Sustainable Development Goals, the first priority should be given to the decarbonization of heating and cooling sectors¹. Nowadays, vapor-compression technology is extensively employed for civil and industry refrigeration, which leads to two serious environmental concerns. On the one hand, billions of running fridges, air conditioning, and heat pump units are swallowing ~25–30% of the electricity, and this demand is expected to continuously grow by several times in the upcoming decades^{2,3}. On the other hand, currently used refrigerants have a thousand-time stronger global warming potential compared to CO₂⁴. For example, the global warming potential of the popular R134a is about 1300 times higher than that of CO₂. Given that such refrigerants with good performance but low global warming potential are very limited⁴, it is urgent to establish a low-carbon refrigeration solution.

Within such a context, solid-state refrigeration technology based on caloric effects becomes a promising alternative. Caloric effects usually include magnetocaloric⁵, electrocaloric⁶, elastocaloric⁷, and barocaloric effects⁸, which characterize the thermal effects during a solid-state phase transition induced by a specific external field, such as magnetic field, electric field, stress, and pressure, respectively. In the entire refrigeration process, the working material stays solid and thus this technology is emission-free and compact^{9–11}. As far as the energy efficiency is concerned, cooling systems working with caloric materials are considerably competitive as expected to reach 60–70% of the Carnot limit or even be 150% more efficient than the vapor-compression refrigeration from the aspect of thermodynamic coefficient of performance^{12,13}.

However, one of the greatest obstacles to the large-scale application of caloric cooling technology is the difficulty that large caloric effects can be only achieved under huge driving fields in current leading materials. For instance, the magnetic fields used to stimulate metamagnetic or magneto-structural transitions in magnetocaloric materials are generally larger than 2 T, which requires heavy and expensive rare-earth-based permanent magnets or superconducting magnets¹⁴. With respect to the electrocaloric materials, the electric fields are in the magnitude of kV m⁻¹ or even MV m⁻¹, which might create breakdown phenomena and hence influence the operation reliability and cycling lifetime¹⁵. In the case of leading elastocaloric materials, the typical driving stress is as large as 700 MPa to obtain good refrigeration performances¹⁶. As for barocaloric materials, the required pressure is usually above 200 MPa for most intermetallics^{17,18} and it is reduced down to about 100 MPa in the recently discovered plastic crystals⁸. Nonetheless, the development of excellent caloric materials with a smaller driving field remains highly challenging.

In this paper, we report a giant barocaloric effect around room temperature in a commercially available ammonium iodide (NH₄I) compound. The phase transition temperature in NH₄I displays high sensitivity to driving pressure, which renders a very small saturation driving pressure and makes NH₄I one of the most efficient and cost-effective caloric materials as estimated by barocaloric strength (maximum isothermal entropy change normalized by driving force). In addition, thorough studies on crystal structures and atomic dynamics using neutron scattering techniques demonstrate that the excellent barocaloric effect is mainly attributed to the configuration entropy changes of [NH₄]⁺ tetrahedra in the frameworks formed by I⁻ ions as well as the large sensitivity of phase transition temperature to external pressure due to the strong coupling between molecular reorientations and lattice vibrations.

Results

Barocaloric effect in NH₄I. The barocaloric effect in NH₄I is studied utilizing differential scanning calorimetry measurements

over the temperature range of 230–340 K, under several constant external pressures (Methods and Supplementary Fig. 2). Following the heat flow data (Supplementary Fig. 2a), a phase diagram is established. As shown in Fig. 1a, a phase transition is observed at ~243 K on cooling or ~268 K on heating under ambient pressure, close to ~257 K obtained by heat capacity measurement¹⁹. A large thermal hysteresis of $\Delta T_{\text{hys}} \sim 25$ K indicates the first-order nature of this phase transition. This phase transition takes place between the intermediate-*T* β -phase (space group *Pm* $\bar{3}$ *m*) and the high-*T* α -phase (*Fm* $\bar{3}$ *m*)²⁰. It is found that the phase transition temperature varies strongly with external pressure. Quantitatively, the steep phase boundary is defined by $dT_t/dP \sim 0.81$ K MPa⁻¹ on cooling while ~ 0.79 K MPa⁻¹ on heating. Although this value is larger than ~ 0.43 K MPa⁻¹ obtained with nuclear magnetic resonance measurement^{21,22}, it is consistent with other thermodynamic and lattice data in this work (next section). It is worth noting that the dT_t/dP are much larger than those of other leading barocaloric materials as summarized in Fig. 1c^{8,17,18,23–39}.

Based on the heat flow data, we obtained the isobaric entropy changes ΔS_t at the phase transition shown in Supplementary Fig. 2b as well as the pressure-induced entropy changes $\Delta S_{P_0 \rightarrow P}$ shown in Fig. 1b. Here, P_0 is the ambient pressure while P is the applied pressure, as described in the previous report⁸. The maximum (or saturated) value of $\Delta S_{P_0 \rightarrow P}(T, P)$ on heating is ~ 71 J K⁻¹ kg⁻¹, which could be realized by a small driving pressure of 40 MPa as shown in Supplementary Fig. 3. This value of $|\Delta S_{P_0 \rightarrow P}^{\text{max}}|$ is comparable to those of other state-of-the-art barocaloric materials (Supplementary Fig. 4a)^{8,17,18,23–39}. The entropy changes in the unit of J K⁻¹ cm⁻³ are also plotted in Supplementary Fig. 4b. The value of 0.21 J K⁻¹ cm⁻³ for NH₄I is also among the largest in inorganic materials. Moreover, the giant dT_t/dP value also opens a wide reversible working temperature window of ~ 41 K under 80 MPa (Supplementary Fig. 3). The pressure sensitivity also gives rise to a giant barocaloric strength, defined by the maximum entropy changes normalized by the saturation pressure, $|\Delta S_{P_0 \rightarrow P}^{\text{max}}/\Delta P|$, which is ~ 1.78 J K⁻¹ kg⁻¹ MPa⁻¹. As summarized in Fig. 1d, the barocaloric strength of NH₄I is much larger than most other barocaloric materials, especially compared with the inorganics. Based on the entropy changes and specific heat capacity⁴⁰, we also estimate the adiabatic temperature via the formula $\Delta T_{\text{ad}} = |T \Delta S_{P_0 \rightarrow P} / C_p|$ ⁴¹, which is ~ 34 K. This is almost ranked as the biggest among the state-of-the-art barocaloric materials as summarized in Supplementary Fig. 4c and Table 1.

In addition to the isobaric measurements, the direct measurements of pressure-induced heat flow were also carried out at 298 K, as shown in Supplementary Fig. 5. Obvious exothermic and endothermic peaks are observed within pressurization (50 \rightarrow 90 MPa) and depressurization (50 \rightarrow 7.5 MPa) processes, respectively. The pressure-induced entropy changes are estimated as 62.7 and 65.6 J K⁻¹ kg⁻¹ for the pressurization and depressurization processes, respectively. These values are in good agreement with the value of 71 J K⁻¹ kg⁻¹ from heat flow measurements under constant pressures shown in Fig. 1.

Phase transitions as a function of temperature. As the origin of the observed barocaloric effect, the phase transition is considered in aspects of crystal structures, reorientation dynamics, and lattice dynamics. According to previous reports, NH₄I undergoes successive phase transitions from low-*T* tetragonal γ -phase (*P4/nmm*) to intermediate-*T* cubic β -phase (*Pm* $\bar{3}$ *m*), and then to another cubic α -phase (*Fm* $\bar{3}$ *m*) (schematic crystal structures are shown in Supplementary Fig. 6)^{20,42}. Our temperature-variable X-ray diffraction (XRD) measurements

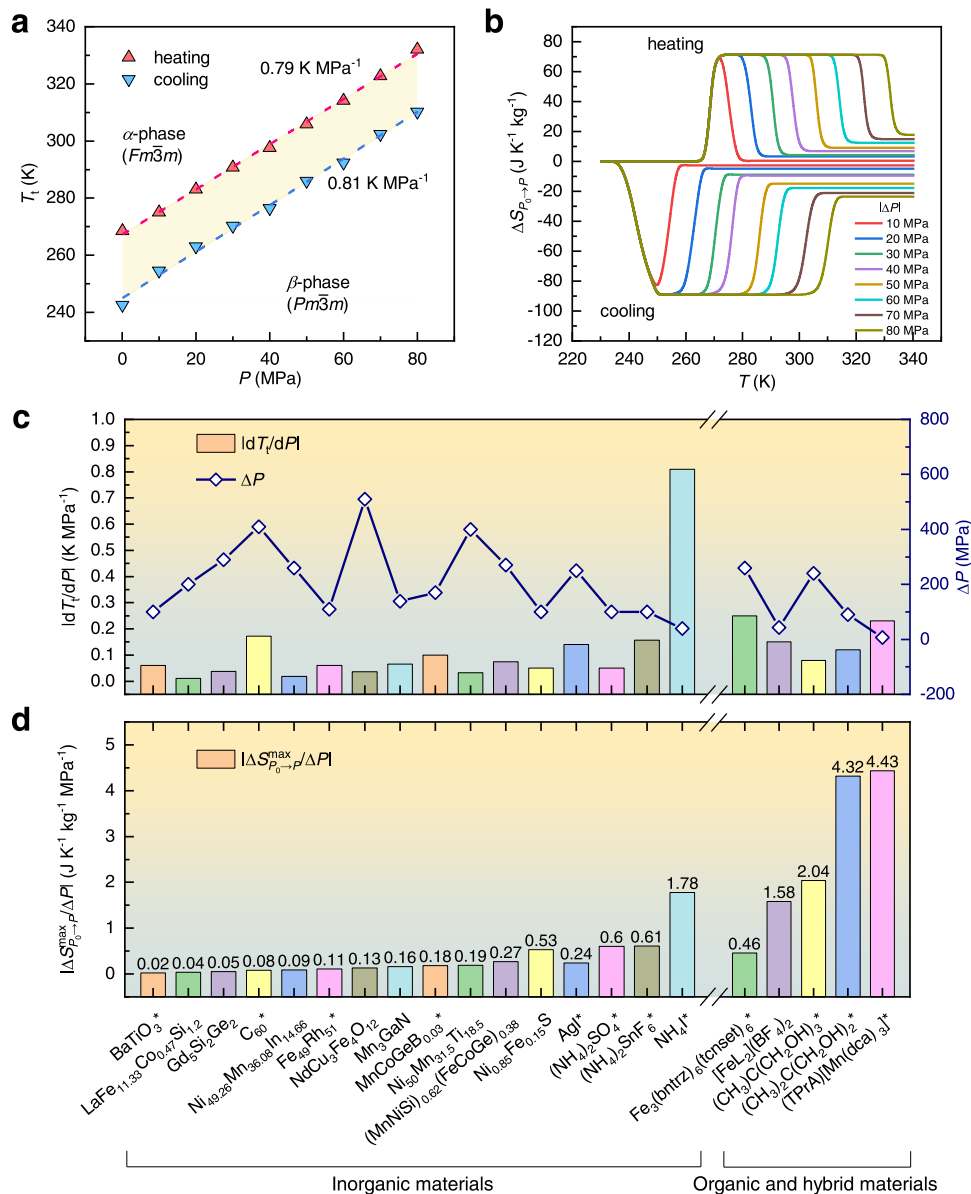


Fig. 1 Barocaloric effects of NH₄I. **a** Phase diagram of NH₄I as functions of temperature and pressure. The cooling (down-triangle) and heating transition (up-triangle) temperatures are derived from calorimetric data in Supplementary Fig. 2a. **b** Pressure-induced isothermal entropy change, $\Delta S_{P_0 \rightarrow P}$, for the cooling and heating processes. **c** Much larger pressure-dependent transition temperature variation $|dT_t/dP|$ and smaller saturation driving pressure compared with other giant barocaloric materials^{8,17,18,23-39}. **d** High barocaloric strength as estimated through $|\Delta S_{P_0 \rightarrow P}^{\max}/\Delta P|$ ³⁴. The data for the samples marked by “*” represents the reversible values with the influence of thermal hysteresis excluded. Details are summarized in Supplementary Table 1.

confirm a first-order phase transition on heating (Supplementary Fig. 7a). The diffraction patterns can be indexed with the β -phase below T_t and α -phase above T_t , respectively. The temperature dependences of lattice parameters are shown in Supplementary Fig. 7b, c. The slope of the temperature dependence of unit cell volume, $(\partial V/\partial T)_{P_0}$, is determined to be 3.3×10^{-8} and $4.23 \times 10^{-8} \text{ m}^3 \text{ kg}^{-1} \text{ K}^{-1}$ for β and α phases, respectively. As a result, the lattice contractions under pressure have a marginal contribution to the total entropy changes for both phases, less than $0.4 \text{ J kg}^{-1} \text{ K}^{-1}$. In addition, the volume change across the $\beta \rightarrow \alpha$ phase transition under ambient pressure is determined to be $\Delta V_t \sim 5.87 \times 10^{-5} \text{ m}^3 \text{ kg}^{-1}$ or 16.95%, which is in good agreement with the value of 16.96% in the literature⁴³. Following the Clausius-Clapeyron equation $\Delta S_t = \Delta V_t / \left(\frac{dT_t}{dP} \right)$, this change corresponds to an entropy

change of $74.3 \text{ J kg}^{-1} \text{ K}^{-1}$, which also agrees well with the experimentally determined value of $\sim 71 \text{ J kg}^{-1} \text{ K}^{-1}$ in Supplementary Fig. 2.

For atomic dynamics, the dynamic structure factor $S(Q, \omega)$ is obtained using inelastic neutron scattering (INS) measurements as a function of energy transfer (ω) and momentum transfer (Q) with the Time-of-Flight Spectrometer, PELICAN, at the Australian Centre for Neutron Scattering (see Methods)⁴⁴. Figure 2a illustrates three typical INS spectra, $S(Q, \omega)$, collected at 160, 260, and 300 K, which correspond to the three phases, respectively. These spectra exhibit different features. At first, the elastic component $S(Q)$ is extracted by integrating $S(Q, \omega)$ over $[-0.3, 0.3] \text{ meV}$. The results are shown in Fig. 2b, c. An obvious phase transition can be found at $\sim 275 \text{ K}$, corresponding to the transition from the intermediate- T β -phase to the high- T α -phase^{20,42}. However, it is quite difficult to identify another phase

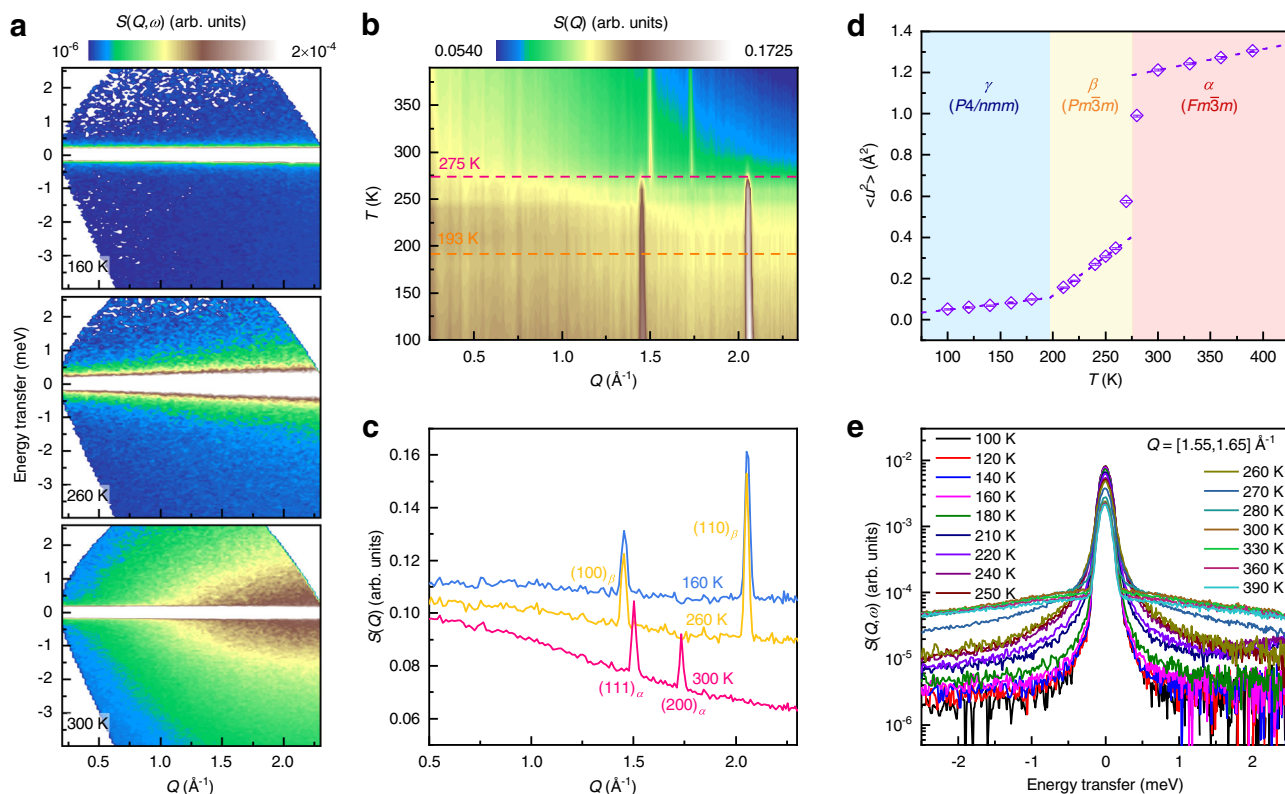


Fig. 2 Phase transitions as a function of temperature in NH_4I . **a** The contour plots of dynamic structure factor, $S(Q, \omega)$, for NH_4I at 160, 260, and 300 K measured at PELICAN with $E_i = 3.72$ meV. **b** The contour plot of elastic structure factor $S(Q)$ as a function of temperature. **c** Comparison of $S(Q)$ at 160, 260, and 300 K. The Bragg peaks for the high- T α -phase and the intermediate- T β -phase are marked with subscripted ' α ' and ' β ', respectively. **d** Experimental mean-squared displacement, $\langle u^2 \rangle$, determined from the fitting of $S(Q)$ to $S(Q) \propto \exp(-Q^2 \langle u^2 \rangle / 3)$ (see Supplementary Fig. 8). **e** Sliced $S(Q, \omega)$ over the Q range of $[1.55, 1.65] \text{ \AA}^{-1}$ as a function of energy transfer.

transition between the low- T γ -phase and the intermediate- T β -phase, as the γ -phase is derived from the β -phase with a tiny distortion^{20,45}.

To accurately track the phase transition, the atomic mean-squared-displacement (MSD) is analyzed with the Debye-Waller factor fitting of the elastic structure factor, $S(Q)$ (see Supplementary Fig. 8)⁴⁶. The obtained MSD as a function of temperature is shown in Fig. 2d. The MSD across the transition of $\beta \rightarrow \alpha$ exhibits an abrupt jump. In addition, it is noted that the temperature dependences of MSD present a crossover at ~ 193 K, which corresponds to the phase transition of $\gamma \rightarrow \beta$. Given that the cross-section of H (80.26 barn) is much larger than those of I (0.31 barn) or N (0.5 barn), the obtained MSD in Fig. 2d mainly reflects the thermal fluctuation behaviors of hydrogen atoms. In fact, the sliced $S(Q, \omega)$ curves over the Q range of $[1.55, 1.65] \text{ \AA}^{-1}$ also show strong broadening above 193 K, and this broadening develops continuously with increasing temperature until 280 K as shown in Fig. 2e. These two temperature points correspond exactly to the phase transition temperatures of $\gamma \rightarrow \beta$ and $\beta \rightarrow \alpha$.

Order-to-disorder transition and reorientation dynamics. The broad peaks centered around 0 meV as observed in Fig. 2a, e are signals of quasi-elastic neutron scattering (QENS). QENS is widely used to study the dynamics of molecular reorientations of hydrogen-contained materials⁴⁷. $S(Q, \omega)$ over the Q range of $[1.55, 1.65] \text{ \AA}^{-1}$ below 190 K could be fitted with a delta function convoluted with the instrumental resolution function plus a linear background (Fig. 3a). This implies that hydrogen atoms in $[\text{NH}_4]^+$ tetrahedra stay in the lattice of the low- T γ -phase, without a jump or rotation in the given energy window, which is in agreement with

the crystallographic analysis based on diffraction data²⁰. In contrast, a good fitting for the spectra above 190 K needs one more Lorentzian component as depicted in Fig. 3b, c, which is indicative of the activated motions of hydrogen atoms in the β - and α -phases.

The relaxation time, τ , of the reorientation modes is estimated by the full width at half maximum (Γ) of the Lorentzian profile with the formula of $\tau = 2\hbar/\Gamma$ ⁴⁸. As shown in the inset of Fig. 3d, the average Γ at 300 K is ~ 4.09 meV ($\tau \sim 0.32$ ps), which is ~ 25 times smaller than the value of ~ 0.16 meV ($\tau \sim 8.2$ ps) for the 260 K spectrum. Therefore, the reorientation mode in the high- T α -phase is ~ 25 times faster than that in the intermediate- T β -phase, in agreement with the previous reports⁴⁹. It is also noted that Γ for both 260 K and 300 K spectra are almost independent of Q , suggesting a localized nature of the reorientation modes similar to perovskite $\text{CH}_3\text{NH}_3\text{PbI}_3$ and nano- NaAlH_4 ^{48,50}. In addition, the activation energies of the reorientation modes are examined by fitting the temperature-dependent $\Gamma(T)$ to the Arrhenius relation. The activation energy of the reorientation modes in the intermediate- T β -phase is 126(5) meV, much larger than 25(1) meV for the high- T α -phase (Fig. 3d).

The ratio between the elastic intensity (integrated area below the delta function) and the total intensity (elastic intensity plus the QENS intensity below the Lorentzian profile) gives rise to the elastic incoherent structure factor (EISF), whose Q dependence reflects the reorientation geometry. Here, several models are employed to reproduce the experimental EISF, including twofold (C_2) and/or three-fold (C_3) jumps, cubic tumbling as well as isotropic rotational diffusion (see Methods for details). As shown in Fig. 3e, f, the C_2 and/or C_3 model can be easily ruled out for EISF at both 260 (β -phase) and 300 K (α -phase). However, the

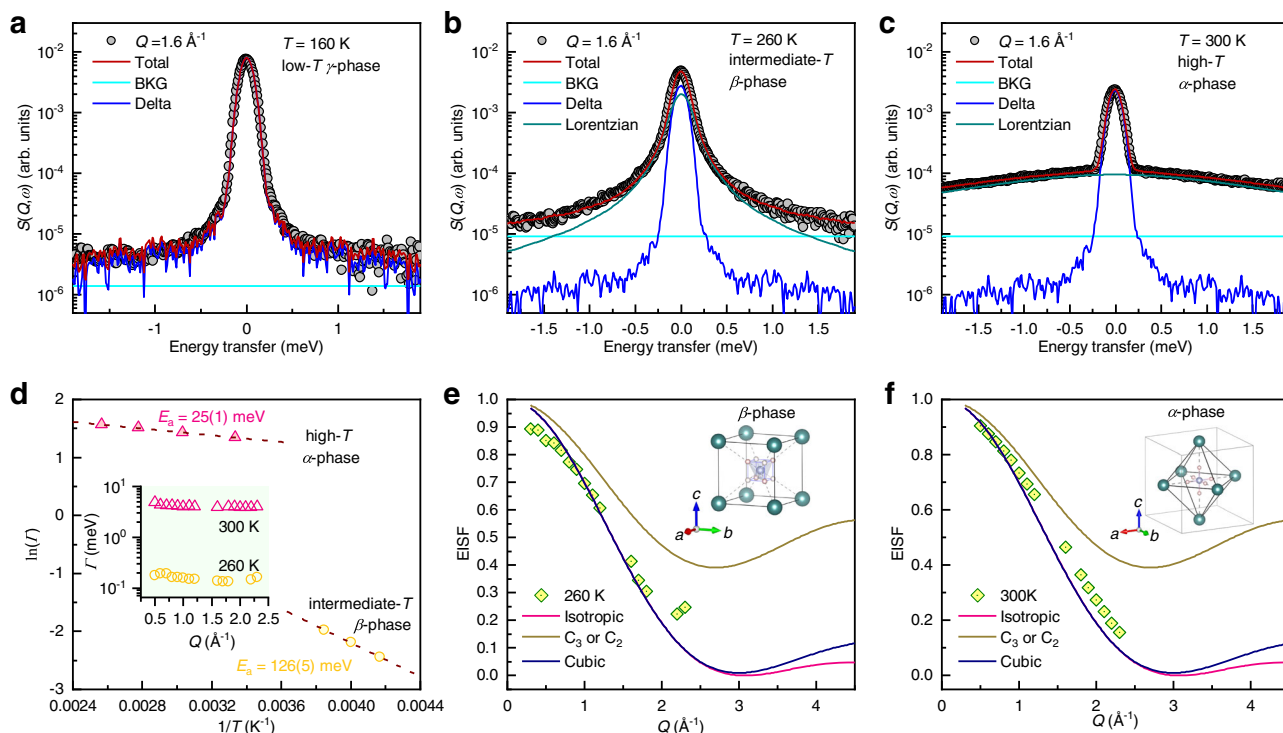


Fig. 3 Reorientation dynamics of ammonia molecule. **a–c** Spectral fitting of the sliced $S(Q, \omega)$ over the Q range of $[1.55, 1.65] \text{ \AA}^{-1}$ at **(a)** 160, **(b)** 260, and **(c)** 300 K, respectively. One constant background (BKG) plus a delta function convoluted with the resolution function could make a good fitting for the spectrum at 160 K, while one more Lorentzian profile is needed at 260 and 300 K. **d** Temperature dependence of the full width at half maximum, Γ , of the Lorentzian components for the intermediate- T β -phase and the high- T α -phase, which are fitted to the Arrhenius equation, $\Gamma \propto \exp\left(-\frac{E_a}{k_B T}\right)$, where E_a is the activation energy for the motions and k_B is the Boltzmann constant. Inset shows Q dependences of the Γ . **e, f** Experimental EISF compared with different reorientation models at 260 and 300 K, respectively. Insets show the schematic diagrams of the coordinations between I^- and $[\text{NH}_4]^+$ ions in the β - and α -phases, respectively. Following the symmetric operations, the hydrogen atoms could dwell on any of the diagonal lines in the β -phases, while the hydrogen atoms residing along the $[100]$ direction would give a sixfold steric distribution in the α -phase (single-approach model, see Supplementary Fig. 6).

EISF can be well reproduced with the cubic tumbling and isotropic rotational diffusion models. It cannot make a clear distinction between these two models due to the limited Q range of the current data.

The reorientations of $[\text{NH}_4]^+$ tetrahedra are restricted by their molecular symmetry as well as the local crystal environment. Therefore, symmetry analysis is also employed for further discussion about the reorientation modes in NH_4I . In the intermediate- T β -phase, the $[\text{NH}_4]^+$ tetrahedron resides in a cube cage formed by eight I^- ions as illustrated in the inset of Fig. 3e. In this geometry, each N–H bond (three-fold axis) of the $[\text{NH}_4]^+$ tetrahedron is aligned with the three-fold axis of the cube cages, so that four N–H...I hydrogen bonds could be built and then lead to an energy minimum. This set leads to a T_d configuration, and the $[\text{NH}_4]^+$ tetrahedra have two orientational freedoms, which match the cubic tumbling model as shown in Fig. 3e^{45,51}. In the high- T α -phase, the reorientation dynamics become more intricate. Each $[\text{NH}_4]^+$ ion is surrounded by six I^- ions, which form an octahedral cage. A lot of models have been proposed in early literatures^{20,52–54}, such as single-approach, double-approach, and triple-approach models⁵² or isotropic model⁵⁴, although no exclusive decision can be made. One common feature of these models lies in that the four tetrahedrally arranged hydrogen atoms cannot achieve a close approach to the octahedrally distributed I^- ions simultaneously⁵². In this work, the single approach is considered, where only one linear N–H...I hydrogen bond is formed (see inset of Fig. 3f or Supplementary Fig. 6c, d). In this configuration, the $[\text{NH}_4]^+$ tetrahedron has six orientational freedoms^{45,51}. This leads to a configuration entropy

change of $63 \text{ J K}^{-1} \text{ kg}^{-1}$ across the $\beta \rightarrow \alpha$ transition (see Methods), close to the entropy change of $71 \text{ J K}^{-1} \text{ kg}^{-1}$ in Fig. 1b.

Strong reorientation-vibration coupling. The neutron-weighted phonon density of states (DOSs) was measured on the NH_4I powder sample at PELICAN (Methods), and the results are shown in Fig. 4. The phonon DOS profile at 160 K contains six well-defined peaks up to 80 meV. According to the previous INS studies, the ~ 4.8 and ~ 7 meV peaks are related to the acoustic (marked as ‘A’) phonon bands, and the ~ 18 meV peak is associated with the optical (marked as ‘O’) phonon band^{55,56}, while the other three optical phonon bands at higher energy range have not yet been reported. However, the corresponding counterparts have been observed in NH_4Br ⁵⁷, although the peak positions exhibit some differences because of the different molecular masses or chemical bonding strengths in NH_4I and NH_4Br . Thus, these three high-energy optical phonon bands would be attributed to the libration motions of the hydrogen atoms in $[\text{NH}_4]^+$ tetrahedra.

One obvious phenomenon about the phonon DOSs is the significant broadening at the transition temperature of ~ 275 K, above which the profiles become featureless. In addition, it is observed that the optical phonon bands, especially the O_{II} , O_{III} , and O_{IV} ones, show dramatic softening with increasing temperature as delineated by the dashed lines in Fig. 4. These two features of the phonon DOSs imply that the lattice vibration potentials of NH_4I are very shallow and anharmonic. In combination with the fact that the hydrogen atoms in $[\text{NH}_4]^+$

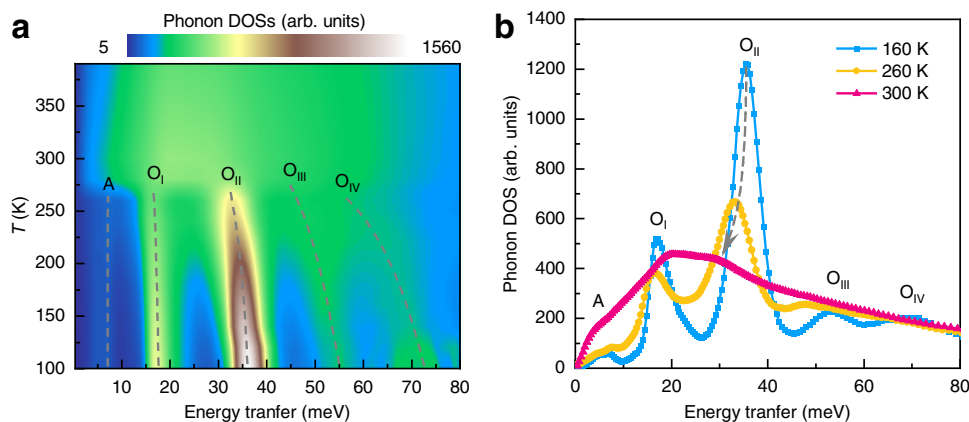


Fig. 4 Variation of lattice dynamics with temperature. **a** Contour plot of neutron-weighted phonon density of states (DOSs) as a function of temperature. **b** The profiles at 160, 260, and 300 K, respectively. The dashed lines are used for guiding eyes to track the variation of the phonon bands with temperature. ‘A’ and ‘O’ denote the acoustic and optical phonons, respectively.

tetrahedra exhibit different reorientation dynamics with the development of phonon anharmonicity (Fig. 3), it can be concluded that NH_4I compound has a strong coupling between molecular reorientations and lattice vibrations, perhaps through the hydrogen bonds between the $[\text{NH}_4]^+$ tetrahedra and their I^- coordination environments. This phase transition dominated by reorientation-vibration coupling in NH_4I can also be understood from the viewpoint of thermodynamics. With increasing temperature, the rising configurational entropy of $[\text{NH}_4]^+$ tetrahedra tends to stabilize the high- T phases, similar to the entropy-driven structural transition in formamidinium lead iodide perovskite⁵⁸.

Responses of dynamic behaviors to external pressure. The responses of the phase transition to external pressure are also studied using INS under different pressures. Shown in Fig. 5a, b are contour plots of $S(Q, \omega)$ under 0.1 and 300 MPa at room temperature, respectively. This comparison becomes clearer in the sliced curves over the Q range of $[1.55, 1.65] \text{ \AA}^{-1}$ as shown in Fig. 5c. The faster (larger Γ) reorientation mode is suppressed to be the slower (smaller Γ) mode. In addition, with the suppression of the faster reorientation mode, two peaks emerge at ~ 19 and ~ 34 meV from the featureless phonon DOS of the high- T α -phase, corresponding to the O_I and O_{II} bands in the intermediate- T β -phase as shown in Fig. 5d. It can be seen that the application of external pressure certainly induces changes in both the reorientation and lattice dynamics. These microscopic dynamic responses to pressure provide a solid standing point for understanding the giant barocaloric effect in NH_4I .

Finally, we would like to emphasize the decisive role of reorientation-vibration coupling in the giant barocaloric effect in NH_4I . Such a coupling is reflected in the simultaneous variations of crystallographic symmetries, anion coordination, mean-squared displacement, lattice dynamics as well as reorientation dynamics, where the $\text{N-H}\cdots\text{I}$ hydrogen bonds between $[\text{NH}_4]^+$ and I^- play the key roles, as suggested in literatures^{59,60}. More straightforward, the pronounced optical phonon softening (reduced phonon frequencies) as observed in Fig. 4 is linked to the weakening of the $\text{N-H}\cdots\text{I}$ hydrogen bonds with increasing temperature. Considering the pressure effect, phonons become hardened due to the compressed lattice volume, which is readily understood even in the quasi-harmonic approximation. At the same time, the reorganized hydrogen bonds with greater strength might suppress molecular reorientations, which gives rise to large entropy changes. The coordination environments are subsequently changed from the six-octahedron configuration to the

eight-cube configuration (Supplementary Fig. 6). Consequently, the intermediate- T β -phase is induced. The energy scales are manifested as the large increase of the reorientation activation energy from 25(1) meV in the high- T α -phase to 126(5) meV in the intermediate- T β -phase (see Fig. 3d). Hence, it is plausible that the giant entropy changes mainly originate from the configurational contribution, and the small saturation driving pressure is rooted in the strong reorientation-vibration coupling.

Discussion

To summarize, we present a thorough study on the inorganic NH_4I compound which exhibits a giant barocaloric effect over a broad temperature range around room temperature. One of the most noticeable features of NH_4I is the giant pressure sensitivity of the phase transition temperature. Although larger entropy change requires smaller dT_t/dP as suggested by the Clausius-Clapeyron equation³³, a larger dT_t/dP value is also desirable in practice for smaller driving pressures as demonstrated in NH_4I . The great pressure sensitivity of the phase transition temperature stems from the strong coupling between molecular reorientations and lattice vibrations, while the giant entropy change is largely contributed by the orientational disorder of $[\text{NH}_4]^+$ tetrahedra. This work is expected to inspire the discovery of giant barocaloric materials with high pressure-sensitive phase transition, and hence push a big step forward towards the realization of efficient and affordable barocaloric refrigeration.

Methods

Sample preparation and characterization. The NH_4I powder sample with 99.999% purity was purchased from Aladdin. The XRD measurement was carried out on a powder sample at a Rigaku Miniflex-600 diffractometer with $\text{Cu-K}\alpha$ radiation over 10° – 90° with a constant step of 0.02° at room temperature (see Supplementary Fig. 1). Temperature-variable XRD patterns were collected on a Rigaku Smartlab diffractometer with $\text{Cu-K}\alpha$ radiation. A polycrystalline sample was cooled down to 175 K, where it was kept for 30 min. Then, the measurements were performed over 175–375 K for every 10 K. All patterns were analyzed with Rietveld refinement method using the FullProf suites⁶¹.

Barocaloric measurements. The heat flow measurements were performed using a high-pressure differential scanning calorimeter, μDSC , Setaram^{8,62,63}. For the constant-pressure measurements as a function of temperature, a powder sample weighted ~ 20 mg was sealed into a high-pressure vessel made of Hastelloy, while an empty vessel was also used as a reference. Desirable hydrostatic pressures were generated and maintained by controlling argon gas pressure through the high-pressure gas panel. The data were collected in the temperature range from 230 to 340 K under the constant pressure of 0.1, 10, 20, 30, 40, 50, 60, 70, and 80 MPa, respectively. A ramping rate of 1 K min^{-1} was used for both the cooling and heating processes. For variable-pressure measurements at room temperature, a powder sample weighted ~ 42 mg was sealed into the Hastelloy vessel. The heat flow variations with time were recorded for the pressurization (50–90 MPa) and

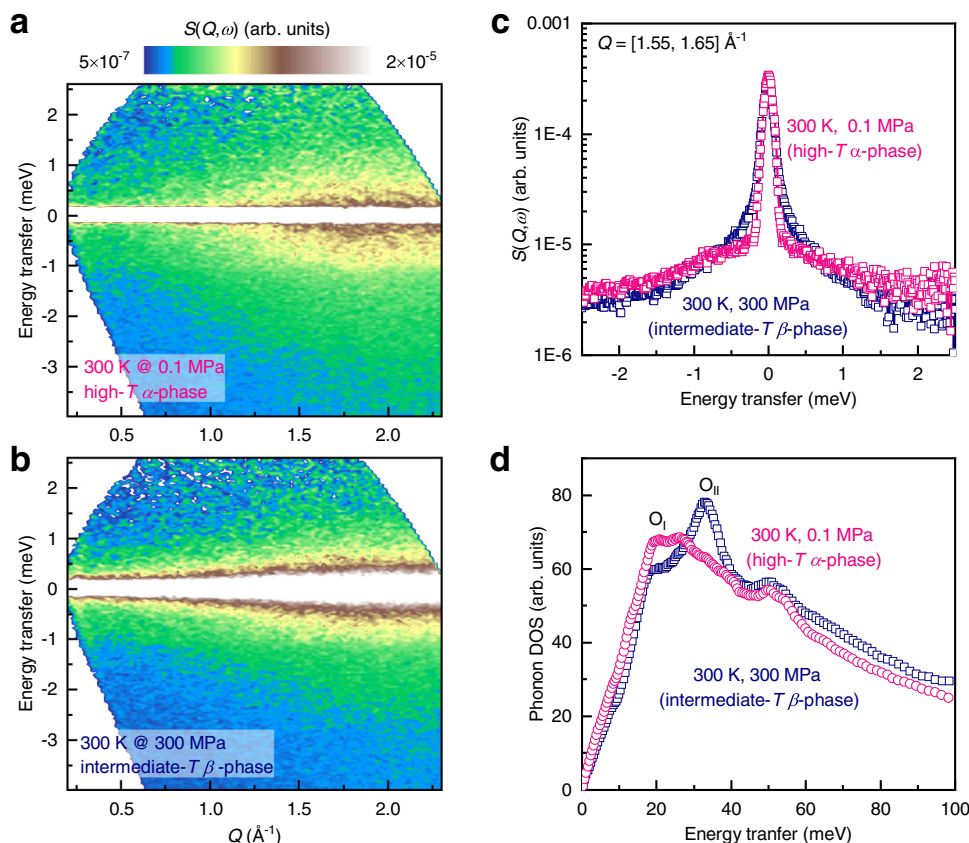


Fig. 5 Responses of dynamic behaviors to external pressure. **a, b** The dynamic structure factor, $S(Q, \omega)$, for NH_4I at 300 K under external pressure of **a** 0.1 MPa (ambient condition) and **b** 300 MPa, respectively. **c, d** Comparison of **c** the $S(Q, \omega)$ sliced over $Q = [1.55, 1.65] \text{ \AA}^{-1}$ and **d** phonon DOSs between the high- T phase (red) and intermediate- T phase (blue) in responses to external pressure.

depressurization (50–7.5 MPa) processes, as drawn in Supplementary Fig. 5. The background was determined by avoiding phase transitions, which was guaranteed by the thermal hysteresis.

INS/QENS measurements. The INS and/or QENS experiments were conducted using the cold-neutron time-of-flight spectrometer, PELICAN, at the Australian Centre for Neutron Scattering, ANSTO⁴⁴. The instrument was configured with an incident neutron wavelength of 4.69 Å, affording incident energy of 3.72 meV with an energy resolution of 0.135 meV at the elastic line. A powder sample was sealed into an annular aluminum can. The measurements were carried out from 100 to 390 K to cover the two-phase transitions. The empty can was measured in the same conditions for background subtraction. In addition, a standard vanadium sample was also measured for detector normalization and determination of the energy resolution function. The high-pressure neutron scattering measurements were performed with the same configuration at 0.1 and 300 MPa at 300 K. A bespoke high-pressure cell made of Be-Cu alloys was used, and a KBr powder sample was employed to calibrate the actual pressures. The data reduction, including background subtraction and detector normalization, was performed using the Large Array Manipulation Program (LAMP)⁶⁴, while the sliced QENS spectra were analyzed in the Pan module built-in the Data Analysis and Visualization Environment (DAVE)⁶⁵.

Analysis of the reorientation dynamics. In the INS spectrum, the broadening underneath the elastic peak is the signal of QENS, which is associated with diffusive and/or reorientation motions. Assuming one single reorientation mode, the QENS dynamics structural factor $S(Q, \omega)$ can be described as⁶⁶:

$$S(Q, \omega) = f \times \left[A_E(Q)\delta(\omega) + \sum A_{QE,i}(Q)L_i(Q, \omega) \right] \otimes R(Q, \omega) + b(Q, \omega) \quad (1)$$

where $\delta(\omega)$ is a delta function representing the elastic peak, $A_E(Q)$ and $A_{QE}(Q)$ are the weights of the elastic and quasi-elastic scattering, f is a scaling factor, $R(Q, \omega)$ is experimentally determined resolution function, and $b(Q, \omega)$ is a linear background. The symbol \otimes describes numerical convolution between the elastic/quasi-elastic components and instrumental resolution. The quasielastically broadened energy

distribution could be well depicted by a Lorentzian function:

$$L(Q, \omega) = \frac{1}{\pi} \frac{\frac{1}{2}\Gamma(Q)}{(\hbar\omega)^2 + (\frac{1}{2}\Gamma(Q))^2} \quad (2)$$

where $\Gamma(Q)$ is the full width at half maximum, corresponding to the frequency of a motion.

To analyze the reorientation geometry of the $[\text{NH}_4]^+$ tetrahedra, EISF was extracted from spectral fitting:

$$\text{EISF} = \frac{A_E(Q)}{A_E(Q) + A_{QE}(Q)} \quad (3)$$

Three models were considered to reproduce the experimentally determined EISF⁶⁷:

C_2 and/or C_3 jumps:

$$\text{EISF} = \frac{1}{2} [1 + j_0(Qd)] \quad (4)$$

Cubic tumbling:

$$\text{EISF} = \frac{1}{8} \left[1 + 3j_0(Qd/\sqrt{2}) + 3j_0(Qd) + j_0(Qd\sqrt{3/2}) \right] \quad (5)$$

Isotropic rotational diffusion:

$$\text{EISF} = j_0^2(Qr) \quad (6)$$

where d is the jump distance, r is the rotational radius, and $j_0(x) = \frac{\sin(x)}{x}$ is the spherical Bessel function of the zeroth order⁶⁷. In the case of NH_4I , d is close to the H–H distance in the $[\text{NH}_4]^+$ tetrahedra ($\sim 1.67 \text{ \AA}$), whereas r is the same as the N–H bond length or $r = d \times \sqrt{3/8}$ ($\sim 1.02 \text{ \AA}$)⁶⁸.

When the possible orientational geometries at a phase transition are determined, the configurational entropies across this phase transition can be estimated by the formula as follows:

$$\Delta S_{\text{conf}} = R \ln \frac{N_2}{N_1} \quad (7)$$

where R is the gas constant, N_1 and N_2 are the numbers of possible orientational configurations below and above a phase transition temperature.

Analysis of the lattice dynamics. The measured dynamic structure factor with powder sample correlates to the phonon DOS, $g(E)^{69}$:

$$g(E) = A \times \left\langle 4M \frac{\exp(-2W)}{\hbar^2 Q^2} \frac{E}{n(E, T) + \frac{1}{2} \pm \frac{1}{2}} S(Q, \omega) \right\rangle \quad (8)$$

where A is a scaling factor, M , and $\exp(-2W)$ are the atomic mass and Debye-Waller factor, respectively, while the '+' and '-' signs denote energy loss or energy gain of neutrons, respectively. $n(E, T)$ is the Bose-Einstein occupation factor, defined as $n(E, T) = [\exp(E/k_B T) - 1]^{-1}$, where k_B is the Boltzmann constant. The brackets $\langle \dots \rangle$ represent the average operator over all Q ranges at a given energy. In a polyatomic material, the experimental determined phonon DOSs are neutron-weighted as⁷⁰,

$$g_{\text{NW}}(E) = \sum_i f_i \frac{\sigma_i}{M_i} g_i(E) \exp(-2W_i) \quad (9)$$

here i represents different elements, f_i is the atomic concentration, $g_i(E)$ is the real partial phonon DOS of the element i . In this work, due to the limited maximum value (~ 3.72 meV) on the energy loss side, only the energy gain side of the $S(Q, \omega)$ up to 80 meV was used to extract the $g_{\text{NW}}(E)$. In addition, it is noted that the values of σ/M for N, H, and I are 0.82, 82.02, and 0.03 barn/amu, respectively. Therefore, the obtained $g_{\text{NW}}(E)$ mainly reflects the vibrational information of hydrogen atoms.

Reporting summary. Further information on research design is available in the Nature Research Reporting Summary linked to this article.

Data availability

The data that support the findings of this study are available from the corresponding author upon request.

Received: 6 February 2022; Accepted: 11 April 2022;

Published online: 28 April 2022

References

- The Royal Society. *Climate change: science and solutions*. <https://royalsociety.org/topics-policy/projects/climate-change-science-solutions/> (2021).
- United Nations Environmental Programme. *The Importance of Energy Efficiency in the Refrigeration, Air-conditioning and Heat Pump Sectors*. https://ozone.unep.org/sites/default/files/2019-08/briefingnote-a_importance-of-energy-efficiency-in-the-refrigeration-air-conditioning-and-heat-pump-sectors.pdf (2018).
- Peters, T. A. *Cool World: Defining the energy conundrum of cooling for all. Technical Report. Birmingham Energy Institute, The Institute for Global Innovation*, <https://www.birmingham.ac.uk/Documents/college-eps/energy/Publications/2018-clean-cold-report.pdf> (2018).
- McLinden, M. O. et al. Limited options for low-global-warming-potential refrigerants. *Nat. Commun.* **8**, 14476 (2017).
- Brown, G. V. Magnetic heat pumping near room temperature. *J. Appl. Phys.* **47**, 3673–3680 (1976).
- Neese, B. et al. Large electrocaloric effect in ferroelectric polymers near room temperature. *Science* **321**, 821 (2008).
- Nikitin, S. A. et al. Giant elastocaloric effect in FeRh alloy. *Phys. Lett. A* **171**, 234–236 (1992).
- Li, B. et al. Colossal barocaloric effects in plastic crystals. *Nature* **567**, 506–510 (2019).
- Hou, H., Qian, S. & Takeuchi, I. Materials, physics and systems for multicaloric cooling. *Nat. Rev. Mater.* <https://doi.org/10.1038/s41578-022-00428-x> (2022).
- Chen, Y. et al. A compact elastocaloric refrigerator. *Innovation* **3**, 100205 (2022).
- Apra, C. et al. Is barocaloric an eco-friendly technology? A TEWI comparison with vapor compression under different operation modes. *Climate* **7**, 115 (2019).
- Maier, L. M. et al. Active magnetocaloric heat pipes provide enhanced specific power of caloric refrigeration. *Commun. Phys.* **3**, 186 (2020).
- Apra, C. et al. The use of barocaloric effect for energy saving in a domestic refrigerator with ethylene-glycol based nanofluids: A numerical analysis and a comparison with a vapor compression cooler. *Energy* **190**, 116404 (2020).
- Kitanovski, A. Energy applications of magnetocaloric materials. *Adv. Energy Mater.* **10**, 1903741 (2020).
- Shi, J. et al. Electrocaloric cooling materials and devices for zero-global-warming-potential, high-efficiency refrigeration. *Joule* **3**, 1200–1225 (2019).
- Cong, D. et al. Colossal elastocaloric effect in ferroelastic Ni-Mn-Ti alloys. *Phys. Rev. Lett.* **122**, 255703 (2019).
- Manosa, L. et al. Inverse barocaloric effect in the giant magnetocaloric La-Fe-Si-Co compound. *Nat. Commun.* **2**, 595 (2011).
- Manosa, L. et al. Giant solid-state barocaloric effect in the Ni-Mn-In magnetic shape-memory alloy. *Nat. Mater.* **9**, 478–481 (2010).
- Stephenson, C. C., Landers, L. A. & Cole, A. G. Rotation of the ammonium ion in the high temperature phase of ammonium iodide. *J. Chem. Phys.* **20**, 1044–1045 (1952).
- Levy, H. A. & Peterson, S. W. Neutron diffraction determination of the crystal structure of ammonium bromide in four phases. *J. Am. Chem. Soc.* **75**, 1536–1542 (1953).
- Andersson, P. & Ross, R. G. The phase diagram of ammonium iodide (NH₄I) under pressure, and a comparison with NH₄Cl and NH₄Br. *J. Phys. C Solid State Phys.* **20**, 4737–4743 (1987).
- Kozlenko, D. P. et al. Ammonium ion dynamics in NH₄I at high pressure. *Mol. Phys.* **99**, 427–433 (2001).
- Stern-Taulats, E. et al. Inverse barocaloric effects in ferroelectric BaTiO₃ ceramics. *APL Mater.* **4**, 091102 (2016).
- Yuce, S. et al. Barocaloric effect in the magnetocaloric prototype Gd₅Si₂Ge₂. *Appl. Phys. Lett.* **101**, 071906 (2012).
- Stern-Taulats, E. et al. Barocaloric and magnetocaloric effects in Fe₄₉Rh₅₁. *Phys. Rev. B* **89**, 214105 (2014).
- Matsunami, D. et al. Giant barocaloric effect enhanced by the frustration of the antiferromagnetic phase in Mn₃GaN. *Nat. Mater.* **14**, 73–78 (2015).
- Aznar, A. et al. Giant and reversible inverse barocaloric effects near room temperature in ferromagnetic MnCoGeB_{0.03}. *Adv. Mater.* **31**, e1903577 (2019).
- Lin, J. et al. Giant room-temperature barocaloric effect at the electronic phase transition in Ni_{1-x}Fe_xS. *Mater. Horiz.* **7**, 2690–2695 (2020).
- Samanta, T. et al. Barocaloric and magnetocaloric effects in (MnNiSi)_{1-x}(FeCoGe)_x. *Appl. Phys. Lett.* **112**, 021907 (2018).
- Aznar, A. et al. Giant barocaloric effect in all-d-metal Heusler shape memory alloys. *Phys. Rev. Mater.* **3**, 044406 (2019).
- Bermudez-García, J. M. et al. Giant barocaloric effect in the ferroic organic-inorganic hybrid [TPrA][Mn(dca)₃] perovskite under easily accessible pressures. *Nat. Commun.* **8**, 15715 (2017).
- Li, J. et al. Reversible barocaloric effects over a large temperature span in fullerite C₆₀. *J. Mater. Chem. A* **8**, 20354–20362 (2020).
- Vallone, S. P. et al. Giant barocaloric effect at the spin crossover transition of a molecular crystal. *Adv. Mater.* **31**, e1807334 (2019).
- Lloveras, P. et al. Giant barocaloric effects at low pressure in ferroelectric ammonium sulphate. *Nat. Commun.* **6**, 8801 (2015).
- Flerov, I. N. et al. Thermal, structural, optical, dielectric and barocaloric properties at ferroelastic phase transition in trigonal (NH₄)₂SnF₆: A new look at the old compound. *J. Fluor. Chem.* **183**, 1–9 (2016).
- Aznar, A. et al. Giant barocaloric effects over a wide temperature range in superionic conductor AgI. *Nat. Commun.* **8**, 1851 (2017).
- Romanini, M. et al. Giant and reversible barocaloric effect in trinuclear spin-crossover complex Fe₃(bntz)₆(tcset)₆. *Adv. Mater.* **33**, 2008076 (2021).
- Aznar, A. et al. Reversible and irreversible colossal barocaloric effects in plastic crystals. *J. Mater. Chem. A* **8**, 639–647 (2020).
- Kosugi, Y. et al. Colossal barocaloric effect by large latent heat produced by first-order intersite-charge-transfer transition. *Adv. Funct. Mater.* **31**, 2009476 (2021).
- Chase, M. W. Jr NIST-JANAF thermochemical tables. *J. Phys. Chem. Ref. Data, Monogr.* **9**, 1–1951 (1998).
- Földeák, M., Chahine, R. & Bose, T. K. Magnetic measurements: a powerful tool in magnetic refrigerator design. *J. Appl. Phys.* **77**, 3528–3537 (1995).
- Durig, J. R. & Antion, D. J. Low-frequency vibrations in ammonium iodide and ammonium bromide. *J. Chem. Phys.* **51**, 3639–3647 (1969).
- Rao, C. N. R. & Natarajan, M. *Crystal structure transformations in binary halides*. (US National Bureau of Standards, 1972).
- Yu, D. et al. Pelican—a time of flight cold neutron polarization analysis spectrometer at OPAL. *J. Phys. Soc. Jpn.* **82**, SA027 (2013).
- Goyal, P. S. & Dasannacharya, B. A. Neutron scattering from ammonium salts. I. Coexisting phases in NH₄I and NH₄⁺ dynamics in phase I and II. *J. Phys. C Solid State Phys.* **12**, 209–217 (1979).
- Telling, M. T. F. et al. Anharmonic behavior in the multisubunit protein apoferritin as revealed by quasi-elastic neutron scattering. *J. Phys. Chem. B* **112**, 10873–10878 (2008).
- Berrod, Q. et al. Inelastic and quasi-elastic neutron scattering. Application to soft-matter. *EPJ Web Conf.* **188**, 05001 (2018).
- Li, B. et al. Polar rotor scattering as atomic-level origin of low mobility and thermal conductivity of perovskite CH₃NH₃PbI₃. *Nat. Commun.* **8**, 16086 (2017).
- Goyal, P. S. & Dasannacharya, B. A. Neutron scattering from ammonium salts. II. Reorientational motion of ammonium ions in octahedral environments. *J. Phys. C Solid State Phys.* **12**, 219–234 (1979).

50. Narase Gowda, S. et al. Quasi-elastic neutron scattering studies of hydrogen dynamics for nanoconfined NaAlH₄. *J. Phys. Chem. C* **120**, 14863–14873 (2016).
51. Guthrie, G. B. & McCullough, J. P. Some observations on phase transformations in molecular crystals. *J. Phys. Chem. Solids* **18**, 53–61 (1961).
52. Levy, H. A. & Peterson, S. W. Neutron diffraction study of the NaCl-type modification of ND₄Br and ND₄I. *J. Chem. Phys.* **21**, 366–366 (1953).
53. Seymour, R. S. & Pryor, A. W. Neutron diffraction study of NH₄Br and NH₄I. *Acta Crystallogr.* **B26**, 1487–1491 (1970).
54. Sharp, A. R. & Pintar, M. M. Nuclear magnetic relaxation study of the establishment of order in the ammonium halides. *Chem. Phys.* **15**, 431–444 (1976).
55. Vagelatos, N., Rowe, J. M. & Rush, J. J. Lattice dynamics of ND₄I in the NaCl phase (I) at 296°K. *Phys. Rev. B* **12**, 4522–4529 (1975).
56. Goel, C. M., Sharma, T. P. & Dayal, B. Lattice dynamics of ND₄I and NH₄I crystals. *J. Phys. Chem. Solids* **38**, 1285–1288 (1977).
57. Goyal, P. S., Penfold, J. & Tomkinson, J. Observation by neutron incoherent inelastic spectroscopy of split higher harmonics of the ammonium ion librational mode in the cubic phase of NH₄Br. *Chem. Phys. Lett.* **127**, 483–486 (1986).
58. Chen, T. et al. Entropy-driven structural transition and kinetic trapping in formamidinium lead iodide perovskite. *Sci. Adv.* **2**, e1601650 (2016).
59. Heyns, A. M., Hirsch, K. R. & Holzapfel, W. B. The effect of pressure on the Raman spectrum of NH₄I. *J. Chem. Phys.* **73**, 105–119 (1980).
60. Huang, Y. et al. Structural properties of ammonium iodide under high pressure. *RSC Adv.* **5**, 40336–40340 (2015).
61. Rodríguez-Carvajal, J. Recent advances in magnetic structure determination by neutron powder diffraction. *Physica B* **192**, 55–69 (1993).
62. Zhang, K. et al. Colossal barocaloric effect in carboranes as a performance tradeoff. *Adv. Funct. Mater.* <https://doi.org/10.1002/adfm.202112622> (2022).
63. Zhang, Z. et al. Barocaloric thermal batteries. Preprint at <https://doi.org/10.48550/arXiv.42103.04348> (2021).
64. Richard, D., Ferrand, M. & Kearley, G. J. Analysis and visualisation of neutron-scattering data. *J. Neutron Res.* **4**, 33–39 (1996).
65. Azuah, R. T. et al. DAVE: A comprehensive software suite for the reduction, visualization, and analysis of low energy neutron spectroscopic data. *J. Res. Natl Inst. Stand. Technol.* **114**, 341–358 (2009).
66. Jalarvo, N. et al. Structure and dynamics of octamethyl-POSS nanoparticles. *J. Phys. Chem. C* **118**, 5579–5592 (2014).
67. Verdal, N. et al. Quasielastic neutron scattering study of tetrahydroborate anion dynamical perturbations in sodium borohydride due to partial halide anion substitution. *J. Alloy. Compd.* **645**, S513–S517 (2015).
68. Andersson, M. S. et al. Interplay of NH₄⁺ and BH₄[−] reorientational dynamics in NH₄BH₄. *Phys. Rev. Mater.* **4**, 085002 (2020).
69. Mittal, R. et al. Effects of magnetic doping and temperature dependence of phonon dynamics in CaFe_{1-x}Co_xAsF compounds (x = 0, 0.06, and 0.12). *Phys. Rev. B* **79**, 214514 (2009).
70. Ren, Q. et al. Establishing the carrier scattering phase diagram for ZrNiSn-based half-Heusler thermoelectric materials. *Nat. Commun.* **11**, 3142 (2020).

Acknowledgements

X.T. and B.L. acknowledge the support by the National Key Research and Development Program of China (Grant No. 2020YFA040600). B.L. also thanks fundings from the Key Research Program of Frontier Sciences of Chinese Academy of Sciences (Grant No. ZDBS-LY-JSC002), CSNS Consortium on High-performance Materials of Chinese Academy of Sciences, the International Partner Program of Chinese Academy of Sciences (Grant No. 174321KYSB20200008), the Liaoning Revitalization Talents Program (Grant

No. XLYC1807122), the Young Innovation Talent Program of Shenyang (Grant no. RC210435) and National Natural Science Foundation of China (Grant No. 11804346). X.T. also acknowledges the financial supports from National Natural Science Foundation of China (Grant No. 11875265), the Scientific Instrument Developing Project of the Chinese Academy of Sciences (3He based neutron polarization devices), Guangdong Basic and Applied Basic Research Foundation (Grant Nos. 2019B1515120079), R&D projects in key areas of Guangdong Province (Grant No. 2019B010941002), and Dongguan Introduction Program of Leading Innovative and Entrepreneurial Talents (Grant No. 20191122). Q.Y.R. thanks the project from National Natural Science Foundation of China (Grant No. 52101236), Guangdong Basic and Applied Basic Research Foundation (Grant No. 2021B1515140014), the Institute of High Energy Physics, Chinese Academy of Science (Grant No. E15154U110), and Open project of Key Laboratory of Artificial Structures and Quantum Control (Ministry of Education) (Grant No. 2021-05). All authors acknowledge the beam time granted by ANSTO (Proposal Nos. 8268 and 8318).

Author contributions

B.L. proposed the project. J.Q., Z.Z., R.S., W.J.R., Z.D.Z., and B.L. carried out in-house structural and thermal characterizations. J.Q. was co-supervised by B.L. and Z.D.Z. Neutron scattering measurements were performed by D.H.Y., Q.Y.R., J.Q., W.L.S., and B.L. The high-pressure cells were prepared by B.Y., Q.Y.R., and X.T. Neutron scattering spectra were analyzed by Q.Y.R. with the help from J.Q., W.L.S., T.H.W., Z.Z., X.T., and B.L. Q.Y.R. drafted the manuscript. All authors edited and finalized the manuscript.

Competing interests

The authors declare no competing interests.

Additional information

Supplementary information The online version contains supplementary material available at <https://doi.org/10.1038/s41467-022-29997-9>.

Correspondence and requests for materials should be addressed to Xin Tong or Bing Li.

Peer review information *Nature Communications* thanks the other anonymous reviewer(s) for their contribution to the peer review of this work.

Reprints and permission information is available at <http://www.nature.com/reprints>

Publisher's note Springer Nature remains neutral with regard to jurisdictional claims in published maps and institutional affiliations.



Open Access This article is licensed under a Creative Commons Attribution 4.0 International License, which permits use, sharing, adaptation, distribution and reproduction in any medium or format, as long as you give appropriate credit to the original author(s) and the source, provide a link to the Creative Commons license, and indicate if changes were made. The images or other third party material in this article are included in the article's Creative Commons license, unless indicated otherwise in a credit line to the material. If material is not included in the article's Creative Commons license and your intended use is not permitted by statutory regulation or exceeds the permitted use, you will need to obtain permission directly from the copyright holder. To view a copy of this license, visit <http://creativecommons.org/licenses/by/4.0/>.

© The Author(s) 2022